energies

MDPI

Article

A One-Dimensional Numerical Model for High-Performance Two-Stroke Engines

Fernando Ortenzi [1,*] and Andrea Bossaglia [2]

[1] ENEA—Italian Agency for New Technologies, Energy and Sustainable Economic Development, 00123 Rome, Italy
[2] IAME Karting, 24040 Zingonia di Verdellino, Italy; a.bossaglia@iamekarting.com
* Correspondence: fernando.ortenzi@enea.it

Abstract: Computer software that simulates the thermodynamic and gas dynamic properties of internal combustion engines can play a significant role in the design and optimization of internal combustion engines. In the present work, a quasi-dimensional numerical model for two-stroke engines is presented. Particular attention was paid to reporting in-cylinder models, combustion (turbulent with flame development and flame–wall interaction), and turbulence (*K-k-ϵ* model), with the addition of tumble- and squish-generated turbulence that is quite common in such engines. The aim was to reduce the role of the calibration constants, which are fundamental for correlating the models with the experiments, and relations for calculating the tumble ratio and turbulent scales were reported. A one-dimensional model for manifolds is also presented (solving the Euler equations), using the second-order Roe Riemann solver with some improvements, paying particular attention to the source terms, such as area variation. Additionally, a new approach to the end-pipe boundaries, which would reduce the mass conservation error, is reported. The engines tested were two kart two-stroke engines, used for racing purposes: the IAME X30 engine and the IAME Screamer III KZ engine. A comparison between the model results and the experimental data was made, and good accordance was observed, with a root mean square error of about 0.5 kW and providing good accuracy in evaluating changes, such as the combustion chamber squish area and the exhaust pipe length.

Keywords: two-stroke engines; combustion; turbulence; 1D gas dynamic model; Riemann solvers

Citation: Ortenzi, F.; Bossaglia, A. A One-Dimensional Numerical Model for High-Performance Two-Stroke Engines. *Energies* **2023**, *16*, 4947. https://doi.org/10.3390/en16134947

Academic Editors: Georgios Mavropoulos, E.C. Andritsakis and Roussos G. Papagiannakis

Received: 8 April 2023
Revised: 25 May 2023
Accepted: 28 May 2023
Published: 26 June 2023

1. Introduction

Computer software is widely used in the design and development process of internal combustion engines; time and cost are the advantages of using such software. Based on the level of detail required, different approaches can be taken. Three-dimensional models offer very highly detailed information on turbulence, combustion, injection, and emissions [1,2]. With recent advancements in computing power and CFD algorithms, 2D and 3D simulations of internal combustion engines are now possible, although they do require a higher computational cost than 1D simulations require. Evidence of this advancement can be found in the references, such as [1,2]. Additionally, recent developments in high-performance computing (HPC) and machine learning (ML) technology have led to the development of ML-accelerated CFD simulations and data-driven surrogates of engines, accelerating the time to achieve solution and design, as seen in references such as [3]. Furthermore, 1D models are a useful tool for quick analysis and performance modeling and have significant advantages in terms of computational time, as seen when they are applied for multi-cylindrical engines with more complex intake ducting, together with turbo-compressor devices. As an example, a one-dimensional model requires about 360 s to run a simulation (for the IAME X30 engine used in the present paper) of 30 iterations for each rpm from 6000 rpm to 16,000 rpm, with a step of 500 rpm. Furthermore, multivariable optimization algorithms can be applied, which provide very useful results when

the purpose is to find the optimal values of engine parameters, such as power and torque. A great deal of the literature addresses the development of such models, mainly for four-stroke engines, from one-zone combustion models to more complex multizone turbulent models [4]; meanwhile, in the work of [5], a very important assessment for the solution of the one-dimensional hyperbolic system of the equations for manifolds can be found. Additionally, some of the literature addresses this with regard to two-stroke engines [6,7], and the works of Blair are among them [7]. There is a significant contribution in tuning, designing, and simulating two-stroke and four-stroke engines, and also a large amount of experimental data for end-pipe discharge coefficients, scavenging empirical models, engine friction, etc., in [7,8], also used in the present work. However, some limitations have been observed in the GPB model [7]; for example, it is a first-order not "shock capturing" scheme which needs iterative cycles in order to resolve the equations for tapered or convergent ducts, which does not allow for supersonic flow in the shock tube, and which does not remove the hypothesis of ideal gases.

Motorsport is one of the sectors in which computer-aided design software can play an important role. Development and calibration tests can be improved, due to the software's considerable advantage in testing engine architecture, with significant reductions in time and cost compared to those of engine test bed experimentation or on-track tests. However, empiricism continues to play a significant role in design and optimization, especially in two-stroke engines. There are still segments of motorsport that continue to use two-stroke engines; their low cost, simplicity, and high specific power ratio make this technology attractive. One of them is professional karting [9], in which karts are mainly powered by these engines, with the exception of rental karts, which may be electric or powered by four-stroke engines. However, they have limits, such as emissions and, importantly, unburnt hydrocarbons. Those emissions, if required, can be controlled with commercial devices, such as automotive catalysts that can reduce them. Moreover, the carbon footprint impact can be reduced by using low-carbon fuels or biofuels, as in four-stroke engines.

In this work, a numerical code was developed, improving that which was presented in [10,11]; in [10], it was applied to four-stroke engines, thus developing an improved multipipe junction model [10]. Additionally, in [11], it was applied to evaluate the mechanical and thermal efficiency of a co-generator. In the present work, this numerical code was applied and tuned in order to simulate the performance of two-stroke engines. This study is focused on the in-cylinder process; in particular, the combustion and turbulent model, and the one-dimensional manifold model, which requires a particular treatment compared to four-stroke engines. The combustion process, as shown in [12], has been modeled in three parts: the first—the early part—is governed by the laminar combustion speed, which grows to become turbulent; the second represents the fully turbulent speed; the last is the end combustion, where the interaction among the head, piston, and cylinder walls reduces the combustion speed and causes it to become laminar [13]. The *K-k-ϵ* turbulence model [14], which accounts for tumble and squish, has been applied to two-stroke engines; it has been refined, using the momentum equation, to calculate the intake energy flowing into the cylinder, with the advantage of reducing the influence of calibration constants, as applied in [14]. A tumble coefficient has also been calculated to be used for two-stroke loop-scavenged engines. Such a calculation reduces, but does not nullify, the need for experimental data and allows the modeling of such engines to take place with a good accuracy. The model has also introduced a refined version of the Riemann solver of ROE, applied to one-dimensional manifolds [15–17], which modifies the source term treatment and, in particular, the area variation term, which is quite common in racing engines, and especially in two-stroke ones. With the improvements developed, such a model is also able to treat abrupt area variations. The pipe end boundaries, when calculated using the method of characteristics, are sources of inaccuracies, especially in mass conservation during backflow.

The IAME X30 125 cc is the low-cost mono-brand engine used for IAME X30 senior and junior karting classes. The latter differs only for the insertion of a restrictor at the exhaust to

decrease the maximum power from about 22 kW to 15 kW. It is a highly successful class with hundreds of drivers in the national championships due to its low cost and maintenance. It has a direct drive (no gearbox), an electric start, and it is derived from 1990s 100 cc kart engines, having three transfer ports, an intake reed valve, and the exhaust silencer inside the exhaust manifold. The KZ 125 cc class represents the maximum expression of karting performances, with a six-speed gearbox and with a maximum power of approximately 37 kW. It has a maximum allowed carburetor diameter limited to 30 mm by regulations, with an intake reed valve, five transfer ports, and three exhaust ports. It also has a limitation in terms of its maximum compression ratio of about 12.3, which limits its maximum power.

This paper is organized as follows: After the present introduction, Section 2 reports the information of the developed model. Section 2.1 analyzes the combustion model in detail, considering early laminar-like combustion, the main combustion process, and the late part influenced by the flame/cylinder walls interaction. The turbulence model is described in Section 2.2: it is a *K-k-ϵ* that accounts for mean flow, tumble flow, squish, turbulence, and its dissipation along with the turbulence scales. Section 2.3 presents the one-dimensional model developed for manifolds, utilizing the ROE model that considers all source terms in the calculation of fluxes and provides an increased accuracy if strong area variations are present. A technique to improve the accuracy on the end pipes modeling is reported in Section 2.4: the method of characteristics, commonly used in boundaries, is a first-order model and can lead to inaccuracies in the presence of surface discontinuities. The results are shown in Section 3, where the results of the model are compared with the experimental data. Finally, the conclusions are outlined in Section 4.

2. Methodology

Two-stroke engines, especially loop-scavenged ones, offer several advantages such as simplicity, compactness, and high specific power. They also lack auxiliaries like valvetrains, so they do not have strong limitations in terms of maximum crankshaft rpm (revolution per minute). Therefore, it is not uncommon for these engines to run at speeds of 16,000 rpm or more. Additionally, the design of the intake and exhaust systems play a crucial role in optimizing engine performance, with the exhaust system featuring a particular shape to maximize the volumetric efficiency. Consequently, it is quite common to find exhaust manifolds with a big variation area optimized for the application where the engine is designed.

In order to develop a model capable of simulating the behavior of such engines, the above characteristics, which are quite different with respect to 4-stroke engines, have to be considered. All the geometries and processes must be reproduced by numerical code and, even if a two-stroke engine seems quite simple, there are numerous phenomena to take into account. The geometry of the intake, transfer, and exhaust ports connected to the cylinder [7] have been represented with a trapezoidal shape smoothed at the angles, so both the intake ports and the exhaust with auxiliary ports can be reproduced realistically. Such ports, during an engine cycle, are totally or partially covered by the piston skirt, and for each piston position, the uncovered area must be calculated.

The geometry and dynamics of the reed valves and stop plates [7,12,18,19] have been simulated as cantilever beams taking into account its interaction with the stop plates. When the pressure at the intake port is higher than the crankcase pressure, the reed valve receives a force that deflects it and then opens the port. The dynamics are modeled using the modal analysis, simulating the first two modes of vibration, and the integration method is the Runge–Kutta 4th order.

When the flow enters in a duct, or passes through the transfer port, reed valve, throttle, etc., the three-dimensional nature of the flow is not taken into account within the one-dimensional model; the effective area of the port is not its geometrical area. Such a problem can be overcome using discharge coefficients unique for each type of boundary device. These coefficients are functions of the area ratio of the port, reed, or throttle, but are functions also of the pressure ratio across the device. Such coefficients are then stored in three-dimensional matrixes, and for each area ratio and pressure ratio, they return as an

output the discharge coefficient. All the data and the procedure to interpolate the tabulated data are taken from [8,18–20].

When the intake and exhaust ports are open (the scavenge process), a model must be developed to calculate the short circuit fraction (the intake mixture, composed by air, fuel, and oil that flows directly to the exhaust), the mixing, and the perfect displacement zones. The scavenge process was modeled following the approach outlined in references [7,19], with two thermodynamic zones (fresh mixture flowing to the cylinder and exhaust gas of the previous combustion), where the volumetric scavenging efficiency (SE_v) is a function of the volumetric delivery ratio (DR_v) as follows [7]:

$$SE_v = 1 - e^{k_0 + k_1 \cdot DR_v + k_2 \cdot DR^2} \tag{1}$$

where the coefficients k_0, k_1, k_2 are empirical and are calibrated with experimental data.

The zero-dimensional objects, such as the plenums, crankcases, and the cylinders, are solved using mass, energy conservation, and a real gas equation to calculate all the thermodynamic parameters. A single thermodynamic zone was used where the above equations are solved [4]:

$$m \cdot c_v \cdot \frac{dT}{dt} = \frac{dh_{in}}{dt} - \frac{dh_{out}}{dt} - \frac{dQ_{ht}}{dt} - P \cdot \frac{dV}{dt} - u \cdot \frac{dm}{dt} \tag{2}$$

$$\frac{dm}{dt} = \frac{dm_{in}}{dt} - \frac{dm_{out}}{dt} \tag{3}$$

$$P \cdot V = m \cdot R \cdot T \tag{4}$$

The cylinder, during combustion and scavenge, is solved using a two-zones thermodynamic model, the fresh mixture, and the exhaust gas. Further details can be found in [4].

The energy equation during combustion for the fresh mixture is:

$$m_m \cdot \frac{dh_m}{dt} = V_m \cdot \frac{dP}{dt} - \frac{dQ_m}{dt} + (h_m - h_{cr}) \cdot \frac{dm_{mcr}}{dt} \tag{5}$$

While for the burned gas, it is:

$$m_b \cdot \frac{dh_b}{dt} = V_b \cdot \frac{dP}{dt} - \frac{dQ_b}{dt} + (h_m - h_b) \cdot \frac{dm_{mcr}}{dt} - (h_{cr} - h_b) \cdot \frac{dm_{bcr}}{dt} \tag{6}$$

$$\frac{dm_{cr}}{dt} = \frac{V_{cr}}{R_{cr} \cdot T_p} \cdot \frac{dP}{dt} \tag{7}$$

The term m_{mcr} is the mass present in the crevices of the combustion chamber, and its derivative represents the flowrate from the cylinder to the crevices and vice versa.

The next three topics will be discussed in detail in the following sections:

- The combustion process: a turbulent combustion model has been developed, taking into account the combustion chamber geometry, turbulence level, and fuel characteristics.
- Turbulence: a *K-k-ϵ* model has been developed to be connected with the combustion model and in-cylinder heat transfer. It takes into account the mean flow, tumble flow, squish, turbulence, and its dissipation together with the turbulence scales.
- One-dimensional gas dynamic flow: in this work, we used a one-dimensional Riemann solver called the Roe model, with some modifications, to take into account the source terms (heat transfer, friction, and pipe area variation) and to enforce the area variation to minimize the mass conservation error.

One of the objectives of the present paper is also to develop combustion and turbulence models that are less dependent on the calibration coefficients, which are not always available, so even though they are present, are set to 1 and the models are tested without the help of the calibration with experimental data.

2.1. Engine Combustion

This section will report all the sub-models developed to model the in-cylinder processes needed to simulate the two-stroke engines, which is the object of is paper.

The gas within the cylinder is treated with a zero-dimensional phenomenological model considering all the processes [4,21].

Once the scavenge phase is completed and the exhaust ports are closed, the compression phase begins. This phase is modeled as a zero-dimensional thermodynamic single zone composed of fresh mixture and a part of the exhaust gases of the previous cycle. The flow (main and turbulent) is also zero-dimensional, incorporating rotating (tumble) flow, squish flow, non-rotating, and turbulent flow. The heat transfer is modeled by taking into account the flow information calculated by the thermodynamic and flow model.

After the spark plug ignition, the cylinder is modeled using a quasi-dimensional two-zones thermodynamic model, the mixture, and the burned zone, with the specification of the flame front and the burning rate with the interaction of the turbulence and the cylinder walls. After the combustion is completed, the expansion phase and finally scavenge will occur.

In the present work, the details of the combustion model and turbulence are reported, while the other sub-models will be reported in the reference section.

The combustion model adopted is a quasi-dimensional two-zone combustion model and is divided in three parts: the first, immediately after the ignition, where the combustion is almost laminar, then a fully turbulent combustion, and finally a part where the interaction between the flame front and cylinder walls influences the burning rate.

The assumption is that the flame front has a spherical shape as is also assumed by [4,22,23], the combustion chamber is spherical with Squish, and, for each piston position and flame front radius, the flame area and the wetted cylinder walls are calculated.

The first phase of the combustion, starting with a speed nearly laminar and growing towards turbulent conditions, has been studied and reported by many authors, and an overview is reported in [12,21]. Between them, the flame development factor (FDF) chosen from the present work is reported in Equation (8) [12,24,25]:

$$FDF = \left(1 - e^{-C_{FDF} \cdot 0.28 \cdot \left(\frac{t}{\tau}\right)^{0.75}}\right)^{0.5} \tag{8}$$

where:

$\tau = \frac{l_T}{u'}$: characteristic time;

l_T: integral scale of the turbulence m;

u': turbulent speed m/s.

where C_{FDF} is a calibration coefficient and t is the time in seconds from spark ignition. There is a large bibliography about turbulent combustion models, composed by Damkohler [26], to fractal-based models [13] and eddy entrainment models [14]; the one used in the present work is that from Gulder [26] (Equation (9)).

$$S_T = v_{lam} + C_S \cdot 0.62 \cdot \left(u' \cdot v_{lam}\right)^{0.5} \cdot {Re_T}^{0.25} \tag{9}$$

where:

C_S is a calibration coefficient;

v_{lam} is the laminar speed m/s;

Re_T is the turbulent Reynolds number.

When the flame front interacts with the combustion chamber walls, another modification of the burning rate must be introduced to take into account this phenomenon.

The correlation used is [13] (Equation (10)).

$$w_{wall} = \frac{A_{lat}^{b}}{A_{lat}^{tot}} \cdot \left(\frac{m_b}{m_{tot}}\right)^{10 \cdot C_{wall}} \tag{10}$$

where:

A_{lat}^{b} is the cylinder wall area wetted by the burned zone;
A_{lat}^{tot} is the total cylinder walls area;
m_b is the burned mass;
m_{tot} is the total mass in the cylinder;
C_{wall} is the calibration coefficient.
The final formula for the combustion speed is:

$$u_T = v_{lam} + C_S \cdot (1 - w_{wall}) \cdot FDF \cdot 0.62 \cdot \left(u' \cdot v_{lam}\right)^{0.5} \cdot {Re_T}^{0.25} \quad (11)$$

while the combustion rate is:

$$\frac{dm_b}{dt} = \rho_m \cdot u_T \cdot A_f \quad (12)$$

where:

ρ_m: mixture density;
A_f: flame front surface area.

In the present work, the default values of the calibration constant, in the absence of more detailed measured data (for example, the measure of the indicated cycle) or 3D CFD data, are all set to 1, as reported in Table 1.

Table 1. Default value for the calibration coefficients used in the present work.

Coefficient	Default Value
C_{FDF}	1
C_S	1
C_{wall}	1

Figure 1 demonstrates the mass burned fraction during the combustion varying the values of the three coefficients, C_{FDF} C_S C_{wall}, influencing the start, the main process, and the end of the combustion.

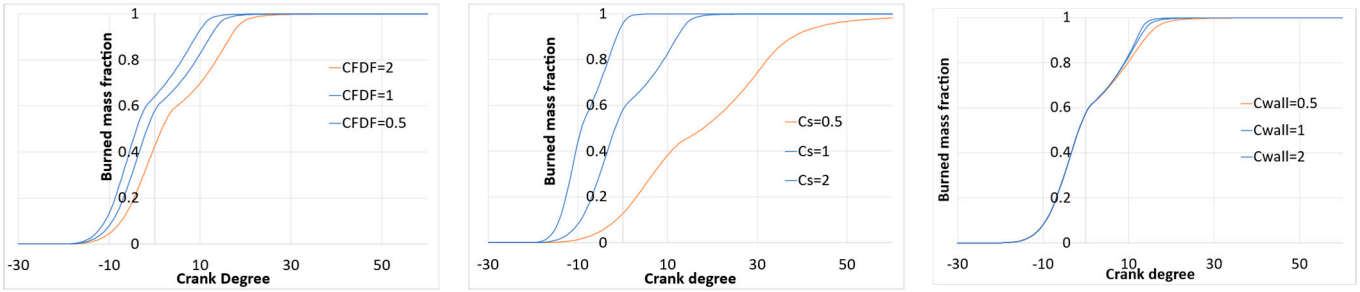

Figure 1. Influence of the calibration constants (C_{FDF}, C_s, and C_{wall}) on combustion (Rpm = 11,500).

The flame surface area, needed to calculate the burning rate, was calculated assuming that the combustion chamber is spherical with a squish band with the spark plug in the center of the chamber, so for each value of the burned mass and volume, the flame radius, the flame area, and the cylinder walls wetted by each zone (burned and mixture) are calculated.

2.2. In-Cylinder Turbulence

The combustion model reported in the previous section requires some information about flow, specifically the turbulence speed u' and the integral scale of turbulence l_T.

Such parameters can be calculated using a turbulence model within the cylinder in all the phases (compression, combustion, expansion, and exhaust/scavenge). The model used, a *K-k-ϵ* model, has the capability to reproduce the mean flow, the turbulent flow, and its dissipation. The mean flow is divided into two parts: the rotating flow (tumble) and the non-rotating flow. The model is well explained in [14,27,28] for four-stroke engines, and in the present work will be extended for two-stroke ones.

The tumble flow is defined as the rotating flow in the cylinder and is calculated using the momentum conservation equation:

$$\frac{dL}{dt} = \sum C_{Tumble} \cdot \frac{dm_{in}}{dt} \cdot vel_{in} \cdot r_{Tumble} - L \cdot \frac{dm_{ex}}{dt} - \tau_f \tag{13}$$

where L is defined as:

$$L = m \cdot vel_{Tumble} \cdot r_{Tumble} \tag{14}$$

m is the mass of the gas present in the cylinder;
vel_{Tumble} is the isentropic speed at the port throat;
The Tumble radius r_{Tumble} is defined in [29].

$$r_{Tumble} = \frac{1}{2} \cdot \min(Bore, H) \tag{15}$$

C_T is the tumble coefficient that represents the fraction of energy that flows into the cylinder imparted to the tumble macro vortex. Generally, in four-stroke engines with poppet valves they are a function of the valve lift, and further details can be found in [14].

During the scavenge phase, in loop-scavenged engines, theoretically, the flow is uniform and occupies half the cylinder area, and when it reaches the cylinder head, it starts to rotate with a diameter equal to the cylinder bore. In this condition, the tumble coefficient, corresponding to the fraction of the energy associated with the tumble flow, is calculated as follows:

$$C_{Tumble} = C_{T0} \cdot \frac{\int_0^{bore/2} A(r) \cdot dr}{bore/2 \cdot A_{Piston}/2} = C_{T0} \cdot \frac{\int_0^{bore/2} 2 \cdot \left(bore^2/4 - r^2\right)^{0.5} \cdot r \cdot dr}{bore/2 \cdot A_{Piston}/2} = 0.4244 \cdot C_{T0} \tag{16}$$

C_{T0} is a calibration constant of the order of unity to be adjusted with experimental data or CFD analysis.

The wall shear torque τ_f is calculated using the following relation [29]:

$$\tau_f = 0.055 \cdot \frac{\rho}{2} \cdot vel_{Tumble}^2 \cdot Re^{-0.2} \cdot A_{Lat} \tag{17}$$

where:

ρ is the gas density;
Re is the Reynolds number $Re = \frac{\rho \cdot vel_{Tumble} \cdot Bore}{\mu}$;
μ is the gas viscosity.
Finally, the production of the turbulent energy due to the tumble flow is:

$$P_{Tumble} = \frac{1}{2} \cdot \omega_{Tumble} \cdot \tau_f \tag{18}$$

where $\omega_{Tumble} = \frac{vel_{Tumble}}{r_{Tumble}}$.

The kinetic energy of the mean flow, non-rotating, is defined as:

$$\frac{dK}{dt} = (1 - \alpha_{in}) \cdot E_{in} - K \cdot \frac{dm_{ex}}{dt} + \frac{2}{3} \cdot K \cdot \frac{\dot{\rho}}{\rho} - P_{Shear} \tag{19}$$

where:

$K = \frac{1}{2} \cdot m \cdot vel_{mean}^2$ is the mean flow kinetic energy;
vel_{mean} is the mean flow speed m/s;
α_{in} is the fraction of incoming energy that enters as turbulent energy, set to 0.1 as suggested in [14]. In [27], instead, the hypothesis has been made that there is no turbulence in the incoming flow.

The incoming kinetic energy E_{in} from the intake manifold (or backflow from the exhaust) is:

$$E_{in} = C_{in} \cdot \sum \left[(1 - C_{Tumble}) \cdot \frac{dm_{in}}{dt} \cdot vel_*^2 \right] \tag{20}$$

where C_{in} is a calibration constant of the order of unity.

The speed value, used to the calculation of the intake speed, vel_*, is not the isentropic speed vel_{in} at the transfer port (or the valve in the 4-stroke engines), but is calculated using the momentum conservation equation:

$$vel_*^2 = \frac{\rho_{in} \cdot vel_{in}^2 \cdot A_{in} - \left(P_{cyl} - P_{in} \right) \cdot A^*_{piston}}{\rho_{in} \cdot A^*_{piston}} \tag{21}$$

where:

$$A^*_{piston} = \begin{cases} A_{piston} \rightarrow for\ 4\ Stroke\ engines \\ \frac{A_{piston}}{2} \rightarrow for\ Loop\ Scavenged\ 2\ Stroke\ engines \end{cases} \tag{22}$$

The parameters with the suffix "in" are referred at the intake port and with "cyl" to the gas in the cylinder. If the term $\left(P_{cyl} - P_{in} \right) \cdot A^*_{piston}$ is neglected, the term vel_*^2 reduces to $\frac{A_{in}}{A^*_{piston}} \cdot vel_{in}^2$, and, for four-stroke engines, is in accordance with the ratio 0.18 reported in [14]. A compressibility term ($\frac{2}{3} \cdot K \cdot \frac{\dot{\rho}}{\rho}$) has also been added in the energy equation that increases it following the work of [30], that correlated the mean flow model better with high-speed engines, and the term $K \cdot \frac{dm_{ex}}{dt}$ is the energy flowing out from the cylinder.

The shear stress term is instead [14]:

$$P_{Shear} = C_\beta \cdot 4 \cdot 0.38 \cdot \nu_t \cdot \frac{K}{L_g^2} \tag{23}$$

where $\nu_t = 0.09 \cdot \frac{k^2}{\epsilon}$ is the turbulent viscosity.

The geometric length scale L_g is assumed to be a function of the maximum port lift, the cylinder bore, and the instantaneous height of the cylinder as follows:

$$L_g = C_{L_g} \cdot \frac{H_{maxLift}}{Bore} \min(0.5 \cdot Bore, H) \tag{24}$$

With C_{L_g}, which is a calibration coefficient of the order of unity for two-stroke engines.

The turbulent kinetic energy, defined as $k = \frac{3}{2} \cdot m \cdot u'^2$, has its equation:

$$\frac{dk}{dt} = \alpha_{in} \cdot E_{in} + P_k - k \cdot \frac{dm_{ex}}{dt} - \varepsilon \tag{25}$$

The production term is the sum of shear stress, the squish, the tumble, and the compressibility terms:

$$P_k = P_{Shear} + P_{sq} + P_{Tumble} + \frac{2}{3} \cdot k \cdot \frac{\dot{\rho}}{\rho} - \frac{2}{3} \cdot \nu_t \cdot m \cdot \left(\frac{\dot{\rho}}{\rho} \right)^2 \tag{26}$$

The squish term can be calculated using the following relation [7]:

$$P_{sq} = \frac{1}{2} \cdot \dot{m}_{sq} \cdot vel_{sq}^2 \tag{27}$$

The rate of the dissipation term of the turbulent kinetic energy is:

$$\frac{d\epsilon}{dt} = \alpha_{in} \cdot E_{in} \cdot \frac{\sqrt{k/m}}{L_g} + P_\epsilon - \epsilon \cdot \frac{dm_{ex}}{dt} - 1.92 \cdot \frac{\epsilon^2}{k} \tag{28}$$

Its production term is:

$$P_\epsilon = 1.44 \cdot \frac{\epsilon}{k} \cdot \left(P_{Shear} + P_{Squish} + P_{Tumble} \right) + \frac{\epsilon}{k} \cdot \left(2 \cdot k \cdot \frac{\dot{\rho}}{\rho} - \frac{2.64}{3} \cdot \nu_t \cdot m \cdot \left(\frac{\dot{\rho}}{\rho} \right)^2 \right)$$

The integral scale of turbulence is then:

$$l_T = 0.09^{\frac{3}{4}} \cdot \frac{(k/m)^{\frac{3}{2}}}{\left(\frac{\epsilon}{m}\right)}$$

Table 2 reports the default values of the calibration coefficients used for all the simulations.

Table 2. Calibration coefficients default values used in the present work.

Coefficient	Value
C_{in}	1
C_{T0}	1
C_β	1
C_{L_g}	1

The results of the turbulent model can be shown in Figure 2.

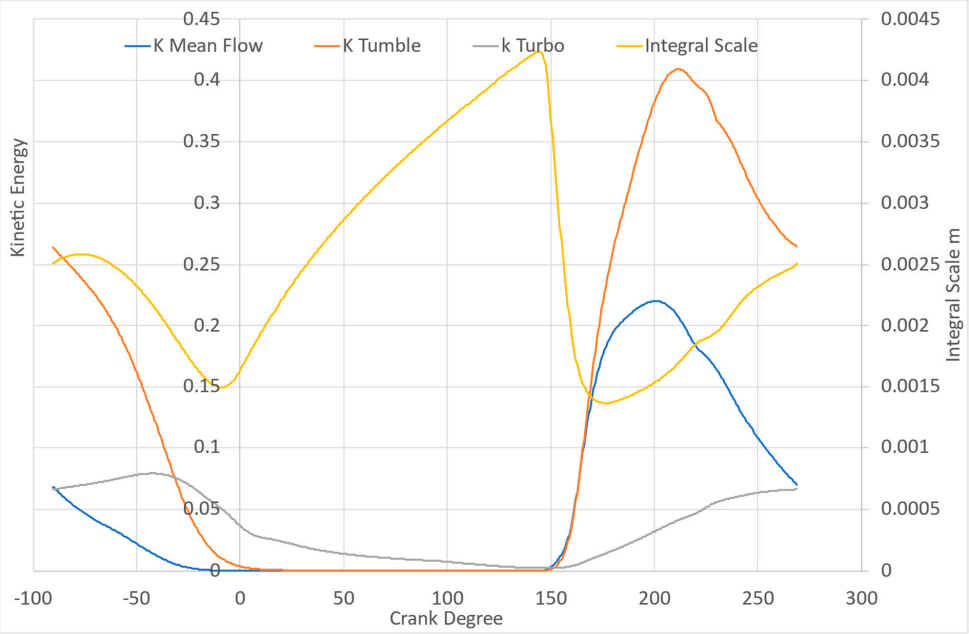

Figure 2. Mean kinetic, tumble, and turbulent energy with the turbulent integral scale during an engine cycle.

2.3. 1D Unsteady Gas Dynamic Model

The performances of two-stroke engines, in terms of torque and power, are much more influenced by the geometry of intake and exhaust manifolds. In racing engines, the optimization of such objects has a very large impact on the performance. The exhaust expansion chamber is one of the examples, with a large area variation, which emphasize the phenomenon of the gas wave actions. Moreover, in the racing application, with high maximum pressure in the cylinders and the exhaust, shocks may be present.

In the present work, a mono-dimensional model was developed and used, with particularly the source terms and the area variation being the most important. The continuity,

momentum, and energy equations that represent the one-dimensional Euler problem are expressed in the following form:

$$\frac{d(A \cdot W)}{dt} + \frac{d(A \cdot F)}{dx} + A \cdot B + C = 0 \tag{29}$$

where the vectors are expressed below:

$$W = \begin{bmatrix} \rho \\ \rho \cdot u \\ \rho \cdot E \\ \rho \cdot X_{air} \\ \rho \cdot X_{fuel} \end{bmatrix} \quad F = \begin{bmatrix} \rho \cdot u \\ (\rho \cdot u^2 + P) \\ \rho \cdot u \cdot \left(E + \frac{P}{\rho}\right) \\ \rho \cdot u \cdot X_{air} \\ \rho \cdot u \cdot X_{fuel} \end{bmatrix} \quad B = \begin{bmatrix} 0 \\ \rho \cdot G \\ -\rho \cdot Q \\ 0 \\ 0 \end{bmatrix} \quad C = \begin{bmatrix} 0 \\ P \cdot \frac{dA}{dx} \\ 0 \\ 0 \\ 0 \end{bmatrix} \tag{30}$$

Such set of differential equations are solved:

$$W_i^{t+dt} = W_i^t - \frac{dt}{A_i} \cdot \frac{(F \cdot A)^*_{i+0.5} - (F \cdot A)^*_{i-0.5}}{dx} - \frac{dt}{A_i} \cdot \frac{S^*_{i+0.5} + S^*_{i-0.5}}{2} \tag{31}$$

With $S^*_{i+0.5} = A_{i+0.5} \cdot B^t_{i+0.5} + C^t_{i+0.5}$.

The source terms are expressed in the form where all the values were known at time t and node i:

$$B^t_{i+0.5} = \frac{B^t_i \cdot A^{0.5}_i + B^t_{i+1} \cdot A^{0.5}_{i+1}}{A^{0.5}_i + A^{0.5}_{i+1}}$$

and

$$C^t_{i+0.5} = \begin{bmatrix} 0 \\ P_{i+0.5} \cdot \frac{A_{i+1} - A_i}{dx} \\ 0 \\ 0 \\ 0 \end{bmatrix} = \begin{bmatrix} 0 \\ \frac{(P \cdot A)_{i+1} - (P \cdot A)_i}{dx} - A_{i+0.5} \cdot \frac{P_{i+1} - P_i}{dx} \\ 0 \\ 0 \\ 0 \end{bmatrix}$$

The closure of the system is made with the assumption of perfect gases, assuming that the internal energy is a polynomial function of the temperature:

$$E = e(T) + \frac{u^2}{2} \qquad P = \rho \cdot r \cdot T$$

The Riemann solver used to calculate the intercell fluxes is that of ROE. The original ROE Riemann solver did not take into account the source terms in the calculation of the fluxes, so that method was not "Well balanced". The addition of such terms [15–17] improved the accuracy, and in this work, has been modified to enforce the area conservation to be more accurate in the mass flow conservation. The new method is now:

$$(F \cdot A)^*_{i+0.5} = 0.5 \cdot \left(F^t_i \cdot A_i + F^t_{i+1} \cdot A_{i+1} - \sum_1^n \alpha_k \cdot |\lambda_k| \cdot e_k \right)$$

Its second-order extension is instead:

$$(F \cdot A)^*_{i+0.5} = 0.5 \cdot \left(F^t_i \cdot A_i + F^t_{i+1} \cdot A_{i+1} - \sum_1^n \alpha_k \cdot |\lambda_k| \cdot e_k \cdot (1 - \varphi(r) \cdot (1 - \nu_k)) \right)$$

where:

$\nu_k = \left| \widetilde{\lambda}_k \right| \cdot \frac{dt}{dx}$, is the local Courant number;

with $r = \frac{\alpha_{k\,upwind}}{\alpha_{k\,local}}$.

Additionally, $\varphi(r)$ is a flux limiter. Among the large number of flux limiters, in the present work, we used the minmod for $r \leq 1$ and the average values between minmod and superbee limiters when $r > 1$ (Figure 3). This model prevents some oscillations when $r \leq 1$ and reduces diffusion for $r > 1$, with the possibility of the Courant–Friedrichs–Lewy number being 0.95.

$$\begin{cases} \varphi(r) = 0 \rightarrow r \leq 0 \\ \varphi(r) = r \rightarrow r \leq 1 \\ \varphi(r) = \min\left(\frac{1+r}{2}, 1.5 \cdot r\right) \rightarrow r > 1 \end{cases}$$

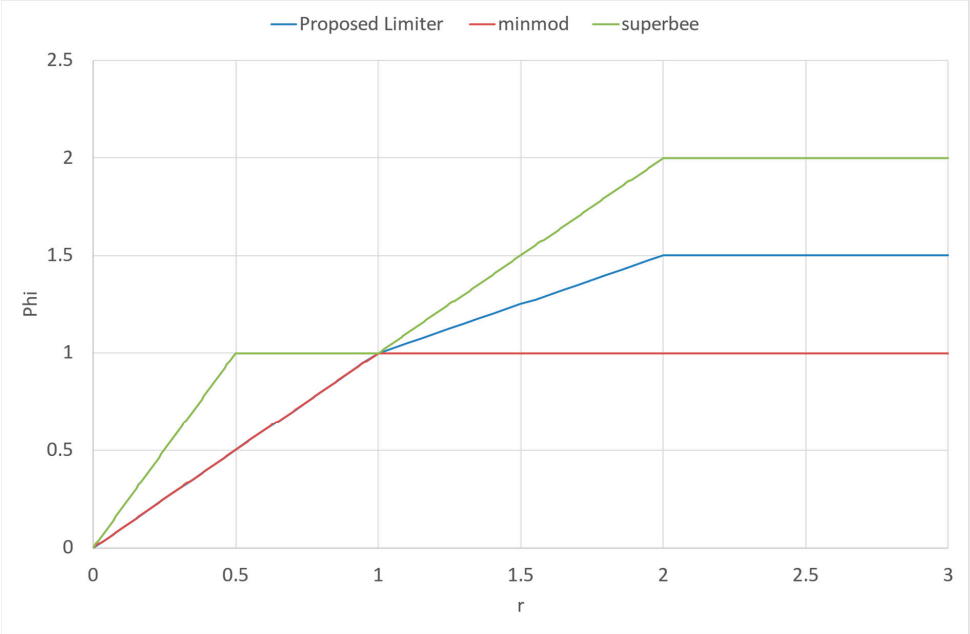

Figure 3. Flux limiter used in the present work.

Setting for the first and the last nodes $\varphi = 1$.

As shown in [31,32], the determination of the average state is crucial to calculate the parameters for the Roe model. In the present work, the area conserved average state is reported to improve the accuracy of the model. The relation used to calculate all the parameters is:

$$d(\rho \cdot u \cdot A) = \rho \cdot A \cdot du + u \cdot d(\rho \cdot A)$$

$$d\left(\rho \cdot u^2 \cdot A\right) = \rho \cdot A \cdot 2 \cdot u \cdot du + u^2 \cdot d(\rho \cdot A)$$

Following the work of [31], these relations reach:

$$\tilde{u} = \frac{\sqrt{\rho_i \cdot A_i} \cdot u_i + \sqrt{\rho_{i+1} \cdot A_{i+1}} \cdot u_{i+1}}{\sqrt{\rho_i \cdot A_i} + \sqrt{\rho_{i+1} \cdot A_{i+1}}}$$

And:

$$\widetilde{\rho \cdot A} = \sqrt{\rho_i \cdot A_i \cdot \rho_{i+1} \cdot A_{i+1}}$$

The value of the density is not known; only its product with an "equivalent area" is known. Neglecting the other calculations for the enthalpy, well reported in [31], all the needed parameters are shown below:

With the definition of $\sigma = \sqrt{\frac{\rho_{i+1} \cdot A_{i+1}}{\rho_i \cdot A_i}}$.

The values of speed, enthalpy, air fraction, and fuel fraction are:

$$\widetilde{u} = \frac{u_i + \sigma \cdot u_{i+1}}{1+\sigma} \; ; \; \widetilde{H} = \frac{H_i + \sigma \cdot H_{i+1}}{1+\sigma}; \widetilde{x_{air}} = \frac{x_{airi} + \sigma \cdot x_{airi+1}}{1+\sigma}; \widetilde{x_{fuel}} = \frac{x_{fuel_i} + \sigma \cdot x_{fuel_{i+1}}}{1+\sigma} \tag{32}$$

The last value to define is the sound speed. In this work, once the enthalpy is known, which is function of the temperature and the gas composition (calculated by Equation (32)), the temperature can be found and then so can the sound speed:

$$\widetilde{a} = \sqrt{\widetilde{\gamma} \cdot \widetilde{r} \cdot \widetilde{T}}$$

with $\widetilde{\gamma}$, $\widetilde{r}$ calculated once T is known from $\widetilde{H}$. This is the most accurate way to calculate it. The values of the speed of the characteristics are:

$$\widetilde{\lambda} = \begin{bmatrix} \widetilde{u} - \widetilde{a} \\ \widetilde{u} \\ \widetilde{u} + \widetilde{a} \\ \widetilde{u} \\ \widetilde{u} \end{bmatrix} \tag{33}$$

This method, as known, violated the entropy condition during transonic expansion [32]. The same author shows a method to avoid this violation with the following relations for left expansion and right expansion:

$$\lambda_{1i} < 0 \text{ and } \lambda_{1i+1} > 0 \rightarrow \overline{\lambda_1} = \lambda_{1i} \cdot \frac{\lambda_{1i+1} - \widetilde{\lambda_1}}{\lambda_{1i+1} - \lambda_{1i}} \tag{34}$$

$$\lambda_{3i} < 0 \text{ and } \lambda_{3i+1} > 0 \rightarrow \overline{\lambda_3} = \lambda_{3i+1} \cdot \frac{\widetilde{\lambda_3} - \lambda_{3i}}{\lambda_{3i+1} - \lambda_{3i}}$$

The α vector is rearranged in the following form, taking into account the source terms like the area variation, friction, and heat transfer:

$$\alpha_k = \alpha_{0k} + \left(\alpha_{areak} + \alpha_{Gk} + \alpha_{Q_k}\right) \cdot \frac{dx}{\lambda_k} \tag{35}$$

Each single term is evaluated below:

$$\alpha_0 = \begin{bmatrix} \frac{\left(A_{i+0.5} \cdot dP - \widetilde{\rho} \cdot A \cdot \widetilde{a} \cdot du\right)}{2 \cdot \widetilde{a}^2} \\ A_{i+0.5} \cdot \frac{\widetilde{a}^2 \cdot d\rho - dP}{\widetilde{a}^2} \\ \frac{\left(A_{i+0.5} \cdot dP - \widetilde{\rho} \cdot A \cdot \widetilde{a} \cdot du\right)}{2 \cdot \widetilde{a}^2} \\ \widetilde{\rho} \cdot A \cdot dx_{air} \\ \widetilde{\rho} \cdot A \cdot dx_{fuel} \end{bmatrix} \tag{36}$$

The average density value is not known, so the area variation term is in the form:

$$\alpha_{area} = \widetilde{u} \cdot \widetilde{\rho} \cdot \frac{dA}{dx} \cdot \begin{bmatrix} 1/2 \\ 0 \\ 1/2 \\ 0 \\ 0 \end{bmatrix} = \widetilde{u} \cdot \left(\frac{d(\rho \cdot A)}{dx} - A_{i+0.5} \cdot \frac{d\rho}{dx}\right) \cdot \begin{bmatrix} 1/2 \\ 0 \\ 1/2 \\ 0 \\ 0 \end{bmatrix} \tag{37}$$

Meanwhile, the heat transfer and friction terms are in Equations (38) and (39).

$$\alpha_{Heat} = \rho \cdot \widetilde{A} \cdot \widetilde{Q} \cdot \begin{bmatrix} -\frac{1}{2 \cdot \widetilde{a}^2} \cdot \left(\widetilde{\gamma} - 1\right) \\ \frac{1}{\widetilde{a}^2} \cdot \left(\widetilde{\gamma} - 1\right) \\ -\frac{1}{2 \cdot \widetilde{a}^2} \cdot \left(\widetilde{\gamma} - 1\right) \\ 0 \\ 0 \end{bmatrix} \text{ with } \widetilde{Q} = \frac{Q_i + \sigma \cdot Q_{i+1}}{1 + \sigma} \tag{38}$$

$$\alpha_{Friction} = \rho \cdot \widetilde{A} \cdot \widetilde{G} \cdot \begin{bmatrix} -\frac{1}{2 \cdot \widetilde{a}^2} \cdot \left[(\gamma - 1) \cdot \widetilde{u} + \widetilde{a}\right] \\ \frac{1}{\widetilde{a}^2} \cdot \left(\widetilde{\gamma} - 1\right) \cdot \widetilde{u} \\ -\frac{1}{2 \cdot \widetilde{a}^2} \cdot \left[(\gamma - 1) \cdot \widetilde{u} - \widetilde{a}\right] \\ 0 \\ 0 \end{bmatrix} \text{ with } \widetilde{G} = \frac{G_i + \sigma \cdot G_{i+1}}{1 + \sigma} \tag{39}$$

The right eigenvector matrix is:

$$\mathrm{e} = \begin{bmatrix} 1 & 1 & 1 & 0 & 0 \\ \widetilde{u} - \widetilde{a} & \widetilde{u} & \widetilde{u} + \widetilde{a} & 0 & 0 \\ \widetilde{H} - \widetilde{u} \cdot \widetilde{a} & \widetilde{H} - \frac{\widetilde{a}^2}{\gamma - 1} & \widetilde{H} + \widetilde{u} \cdot \widetilde{a} & 0 & 0 \\ \widetilde{x_{air}} & \widetilde{x_{air}} & \widetilde{x_{air}} & 1 & 0 \\ \widetilde{x_{fuel}} & \widetilde{x_{fuel}} & \widetilde{x_{fuel}} & 0 & 1 \end{bmatrix} \tag{40}$$

Figure 4 reports the mass flowrate of two tests of the model which has been developed; the first is a sudden area variation and the second is a shock tube. The first, with a manifold of the length of 1 m and a diameter of 0.05 m at the left (with a pressure at the end of 1.8 bar) and 0.1 m at the right (with a pressure at the end of 1 bar), shows the results of the simulation of 2 ducts connected at boundaries with the method of the characteristics [4,33] through the sudden area variation model taken as a reference. The results, with the original Roe method (not balanced), the balanced version [15,16], and the present method, are also reported. When comparing the different results, complete correspondence between the present method and that taken as a reference is highlighted; meanwhile, the other two methods show unrealistic values for the central part of the manifold. The right part of Figure 4 shows the shock tube test where, instead, having lower area variation results means that there is better correspondence between the present method and the balanced version.

2.4. End Pipe Boundaries

The model exposed in the previous section can simulate the wave actions within the pipe in a satisfactory manner, but it is not able to solve the problems at the first and last node of any duct. In such nodes, the method of characteristics is used, while in [15,16], all the pipe ends are modeled. Unfortunately, this is a first-order method, and the accuracy is lower than the second-order method used in the other nodes of the manifold. Additionally, in the case of backflow, when there can be temperature and density discontinuity, the accuracy is even lower. The linear interpolation method, used in the method of characteristics, fails when discontinuity is present. An interesting solution to overcome this inaccuracy is reported in [34] where at the end of the manifolds, an extra-node of half-length was added and applied to the "Two Step Lax-Wendroff" model.

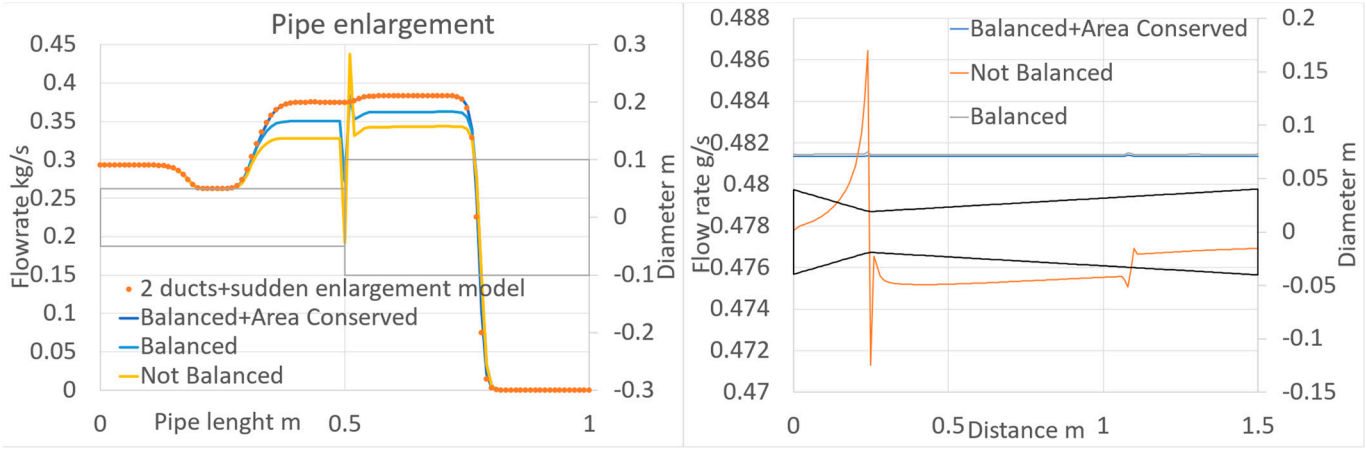

Figure 4. Comparison between the original Roe method, with its balanced version and the present work, for a duct with a sudden enlargement (**left**) and shock tube (**right**) of the mass flowrate.

Below, a solution is proposed for the worst condition that may occur during backflow, such as at the opening of the transfer port for two-stroke engines, but also at the opening of the intake valves in four-stroke engines. When the gas enters the manifold, with a density which is generally different from that present in the duct, a path line will be used, calculating the distance from the end of the duct:

$$dx^*_{t+dt} = dx^*_t + \frac{dx^*_t}{dx} \cdot vel^{i-1}_t + \left(1 - \frac{dx^*_t}{dx}\right) \cdot vel^i_t \tag{41}$$

a value of density at the intermedial node can be calculated:

$$\rho^{i-0.5}_t = \left(1 - \frac{dx^*_t}{dx}\right) \cdot \rho^i_t + \frac{dx^*_t}{dx} \cdot \rho^{i-1}_t$$

An "average density" value of the volume between the node $i-1$ and i is:

$$\rho^{avg}_t = \frac{1}{3} \cdot \rho^i_t + \frac{1}{3} \cdot \rho^{i-0.5}_t + \frac{1}{3} \cdot \rho^{i-1}_t \tag{42}$$

Now the ρ^{i*}_t can be recalculated using the linear interpolation (Figure 5):

$$\frac{\rho^{i-0.5}_t + \rho^{i*}_t}{2} = \rho^{avg}_t$$

and then:

$$\rho^{i*}_t = 2 \cdot \rho^{avg}_t - \rho^{i-0.5}_t \tag{43}$$

This "corrected" value of density can be used to calculate the interpolated values of the sound speed a and the entropy level A_a. To evaluate the benefits of adopting this technique, the error between the inflowing and outflowing mass flowrate has been calculated:

$$Err\% = \sum_0^{360} \frac{\dot{m}_{in} - \dot{m}_{out}}{\dot{m}_{in}} \cdot 100$$

The results of this end pipe correction can be observed in Figure 6, where the flowrate errors of the main transfer manifold of the IAME X30 engine are reported. Such errors can also be of about 2%, and the worst results can be observed at lower and higher rpms, while with the proposed method, the maximum error is about 0.5%.

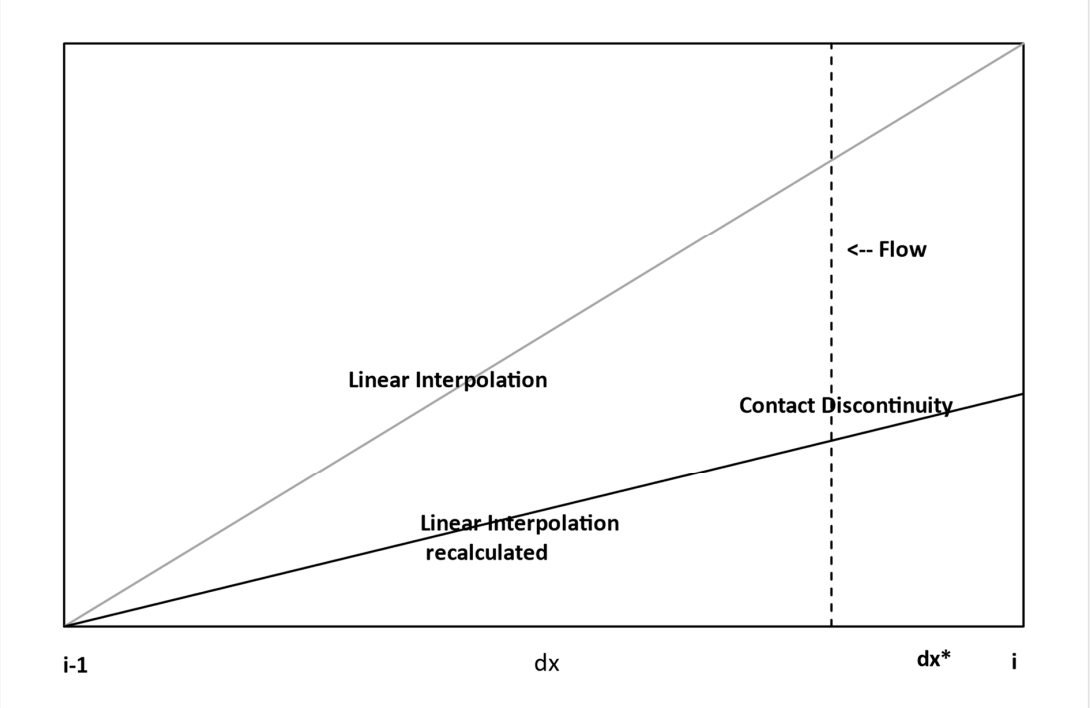

Figure 5. Discontinuity encountered during backflow at the end of a manifold. Linear interpolation and linear interpolation recalculated to reduce the mass error.

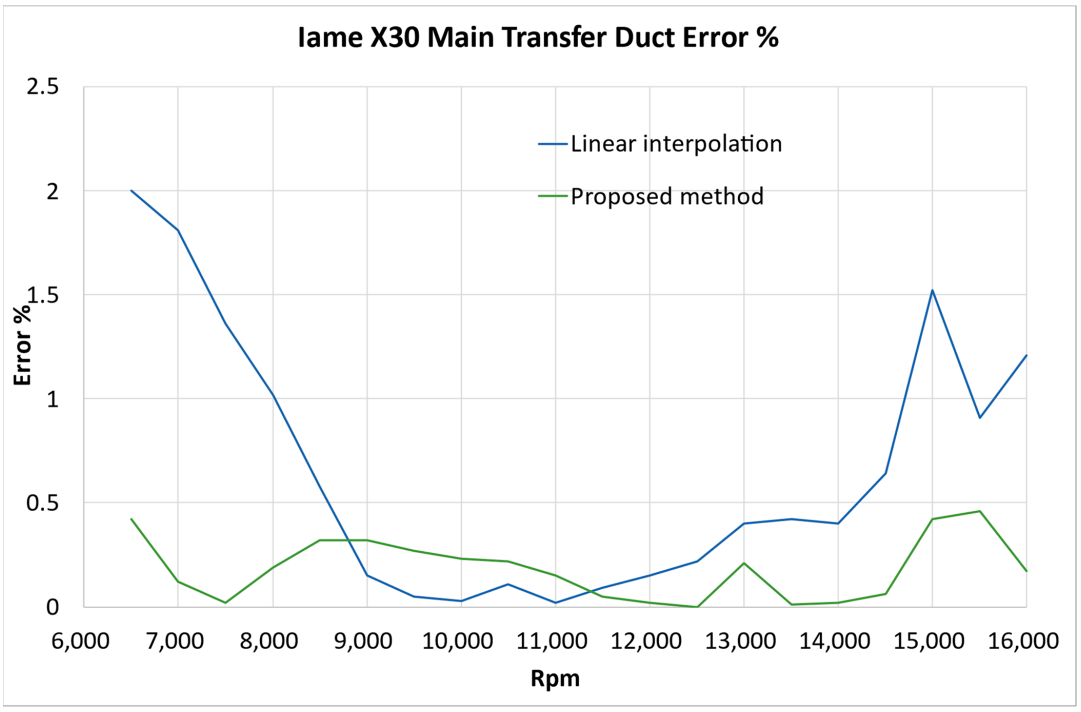

Figure 6. Comparison between the mass conservation error % for the classical linear interpolation and the interpolation corrected for a simulation from 6500 to 16,000 rpm with the IAME X30 engine.

3. Results—Engine Simulations

Internal combustion engine models are nowadays an important tool in the design and development phase of engines, from the optimization of intake and exhaust systems [35]

to the evaluation of the effects of the combustion chamber [22] and also to alternative and blended fuels [36,37].

In this section, the results of the developed numerical code are compared with the experimental results. Such results consist of the measurement on an engine test bed of the power curve, which is the main output of a racing engine. Two engines are tested: the direct drive mono-brand IAME X30 engine and a gearbox engine for the KZ category (IAME Screamer III); both have karting applications, where two-stroke engines continue to exist.

3.1. Engine 1: IAME X30 Series Kart Engine

The X30 series is a mono-brand class 125 cc reed valve, with a fixed regulation, with limited modifications allowed to the tuners. With more than 190 national events taking place under the IAME series flag, there are over 45 international events that IAME attends as a factory and over 135 international events where we participate as partners, making IAME's event calendar one of the most crowded. Together with the strong and widespread participation of motorsport enthusiasts, IAME boasts unparalleled visibility.

The engine has a direct drive transmission and, with a fixed transmission ratio, the range in terms of rpm usage is quite large, from 6500 up to 16,000, limited with an electronic ECU. This has an influence on engine timing, on the design of the exhaust system, and on the combustion chamber design, with a particularly high squish area, higher than the engine with the gearboxes. Another characteristic of this engine is that it has only three transfer ports (Figure 7). The homologation form of the engine, with its specification, is reported in [38], while a picture of the engine is shown in Figure 8.

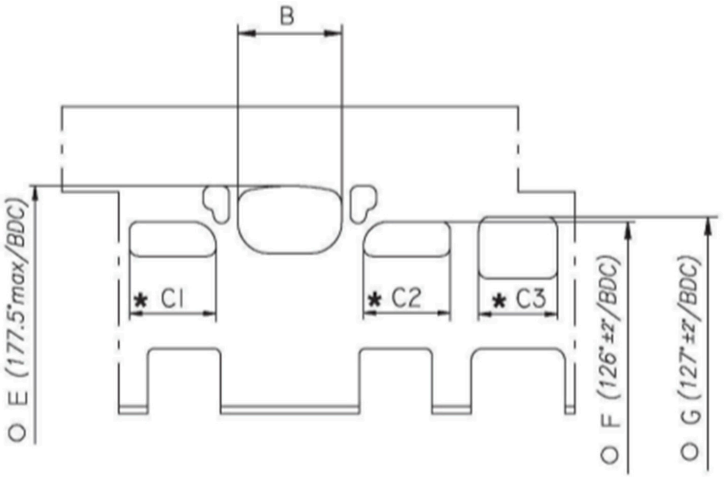

B	≤ 36.5 mm
C1 = C2	≤ 30 mm
C3	≤ 28.5 mm
E	177.5° max
F	126° ± 2°
G	127° ± 2°

Figure 7. Cylinder development of the IAME X30 engine [38].

Figure 9 reports the carburetor and the exhaust system. The carburetor is a Tillotson HW27A that allows the fuel flow to be changed in real-time by the driver with just two screws. During the simulations, the l value was set to 0.85 and the ignition timing was set to 22 crank angle degrees before the top dead center. With the same engine, two configurations are possible, one for the "senior" class, and the other, with a restrictor from 39 mm to 22.7 mm in the exhaust manifold to reduce the power, for the "junior" class. As shown in the above figure, in the tapered part of the exhaust manifold, the diameter does not vary linearly with the length but rather its behavior is more than linear, which is quite common in modern two-stroke engines; during pipe discretization, this must be taken into consideration.

The comparison of the measured and simulated power curve for the senior and junior class is reported in Figure 10. There is quite a good correlation with the experimental data in both of the engines, with a root mean square error of about 0.5 kW.

TECHNICAL DATA	
MODEL	X30 125cc
DESCRIPTION	Single cylinder – 2 stroke
CLASS	125cc Stock Class
BORE	Ø 54.00mm
MAX. BORE	Ø 54.28mm
STROKE	54.00mm
DISPLACEMENT	123.67cc
PORTS	3
INLET SYSTEM	Reed Valve
LUBRICATION	Oil mixture
IGNITION SYSTEM	Digital
TRANSMISSION	Centrifugal Dry Clutch
COOLING SYSTEM	Water
BALANCER SHAFT	Present
STARTER	Electric
CARB. MODEL	Tillotson HW-27A
MAX. POWER	30 Hp
MAX. TORQUE	19.5 Nm
MAX. RPM LIMIT	16.000 RPM

Figure 8. The IAME X30 engine and its specification [38].

The calculated burning durations, 0–10%, 10–90%, and 90–100%, are reported in Figure 11, together with the delivery ratio by volume and mass. The ability to evaluate the influences in terms of the performances of the engine parameters has been tested with two selected parameters: the first is the squish area ratio, that can appreciate the accuracy of the turbulence and combustion model, while the second is the variation in the exhaust length, which is very important when designing and tuning the exhaust system of a racing two-stroke engine.

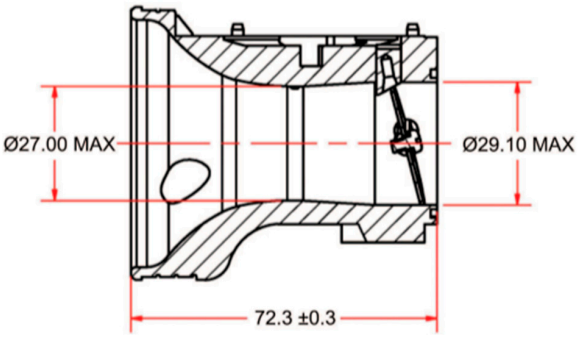

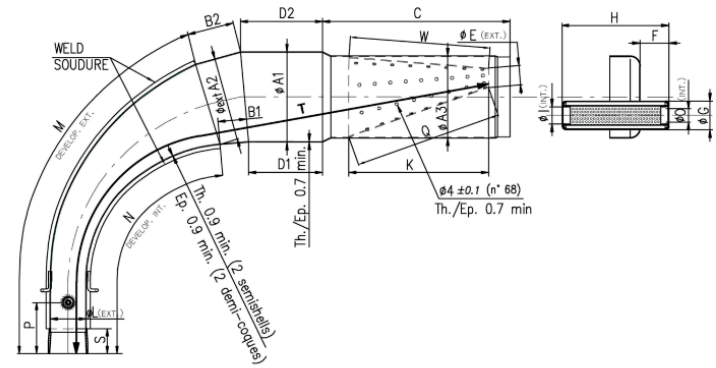

ØA1: 110 ±1.5 Øext.	B2: 60 ±3	ØE: 23.5 ±2 Øext.	ØI: 21 ±1 Øint.	N: 341 ±3	T: 690 ±3
ØA2: 102 ±1.5 Øext.	C: 219 ±3	F: 36 ±2	K: 170 ±3	ØO: 21 ±1 Øint.	W: 170 ±3
ØA3: 100 ±1.5 Øext.	D1: 90 ±3	ØG: 35 ±1 Øext.	ØL: 42.5 ±1.5 Øext.	P: 50 ±10	Q: 182 ±3
B1: 60 ±3	D2: 109 ±3	H: 132 ±3	M: 439 ±3	S: 29 ±1.5	

Figure 9. Geometry of the carburetor (**left**) and the exhaust system (**right**) of the IAME X30 Engine [38].

3.1.1. Squish Area Variation

The combustion chamber of a two-stroke engine is generally quite simple; it has a hemispheric shape with a squish band. The squish band is very often used to improve the turbulence of the mixture, with benefits in terms of combustion speed, which is much appreciated, especially at high engine speeds. The simulations reported here are made by fixing the compression ratio (and then the combustion chamber volume) and varying the squish area band. Two main effects can be observed: by increasing the squish effect,

the turbulence level is increased proportionally to the engine rpm, so, consequently, the combustion duration is lower, but there is a lower bowl in the cylinder head to contain the same volume, meaning that the height of the combustion chamber is higher. The maximum distance from the spark plug to the end of the combustion chamber is then higher with a greater distance to travel for the combustion flame to complete combustion, which means that there is a higher combustion duration. In addition, an increased value of the squish area increases the wall surface and then the heat transfer with a loss of efficiency. The sum of these effects is shown in Figure 12.

At lower rpm, the squish has a lower effect, so when increasing the squish area band, the combustion duration (from 10% of the fresh air burned to 90) increases up to 4–5 degrees from a 0% to 65% area. This difference is reduced by increasing the rpm, and at about 13,500, is null (comparing 0% squish with 65%). At the highest rpm, the combustion chamber with higher squish has a lower combustion duration. This suggests that higher values of the squish area are a benefit for engines that run at a high rpm. There is also a lower variation in terms of the combustion duration from a low to high rpm that allows the optimal ignition value to advance for a higher rpm range.

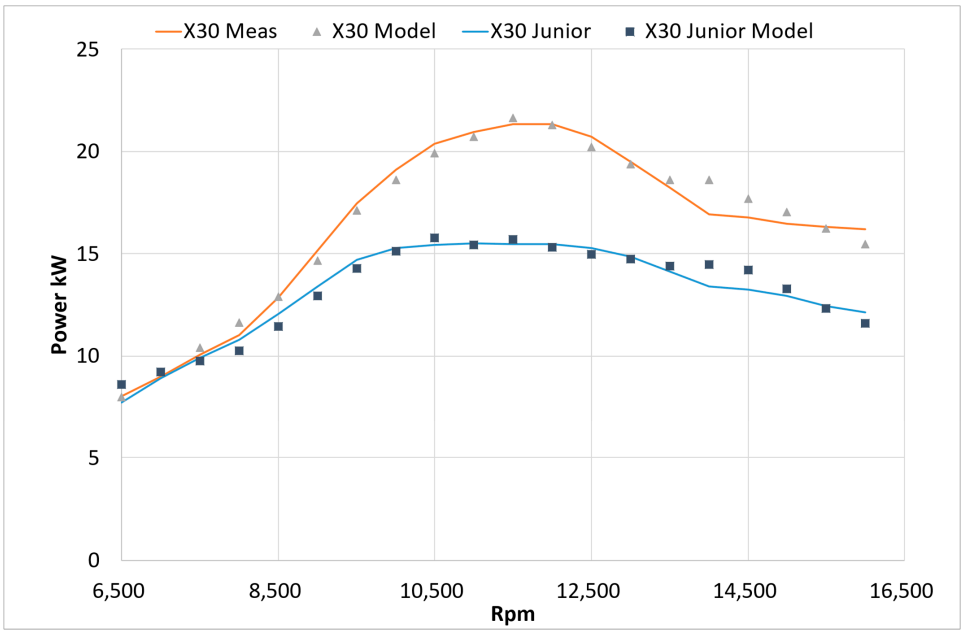

Figure 10. Comparison between measured results of X30 engines (senior and junior class) with the model results.

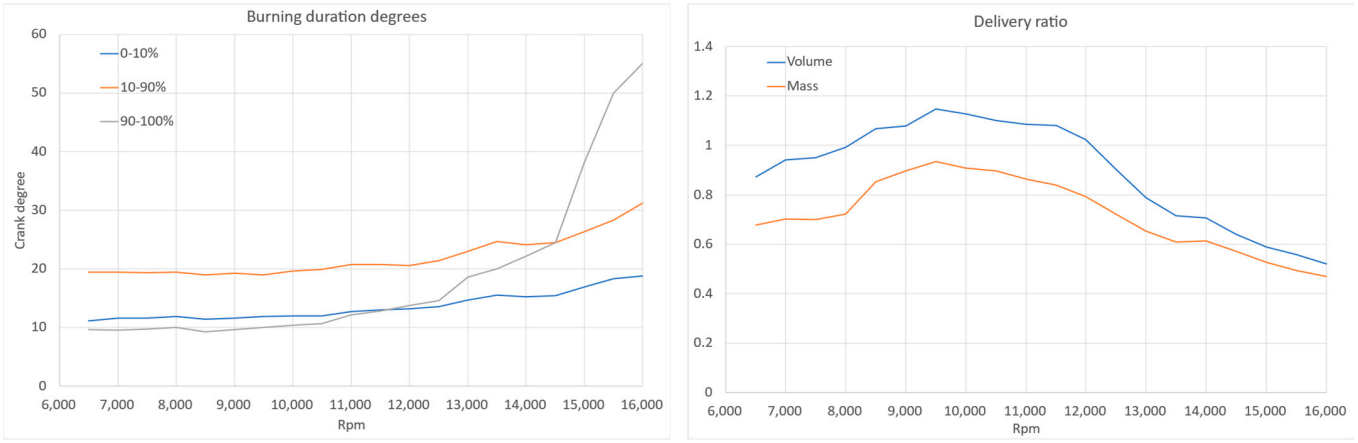

Figure 11. Burning duration and delivery ratio in function of Rpm for the IAME X30 engine.

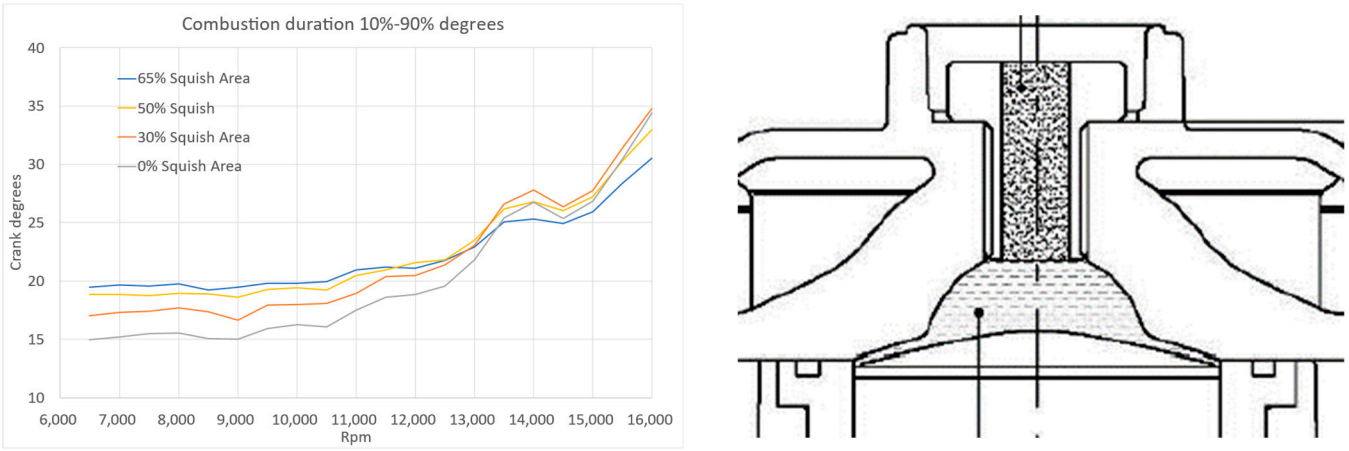

Figure 12. Combustion duration in crank angle degrees (10–90%) for different values of the squish area for the IAME X30 engine (**left**) and the engine head drawing (**right**) [38].

3.1.2. Exhaust Length

The exhaust system of a two-stroke engine plays a fundamental role in its performance, where also variations of some millimeters can induce large modifications to the power curve. The IAME X30 series is a stock class with a limited possibility to tune the engine, but one of them is to change the length of the exhaust system by adding or eliminating some gaskets immediately after the cylinder block (Figure 13). Generally, the exhaust system is optimized to produce a backward expansion pressure wave that improves the scavenging process and a backward compression wave that improves the volumetric efficiency at the end of the scavenging phase. The expansion wave is produced by the tapered cone at the center of the exhaust manifold, while the compression wave is produced by the end cone (that in the present engine is inside the silencer). The length and diameter of each part of the manifold are perfectly optimized, and each variation provides non-negligible differences in terms of performance. For example, longer exhaust systems are suited for engines that run at low rpm and vice versa.

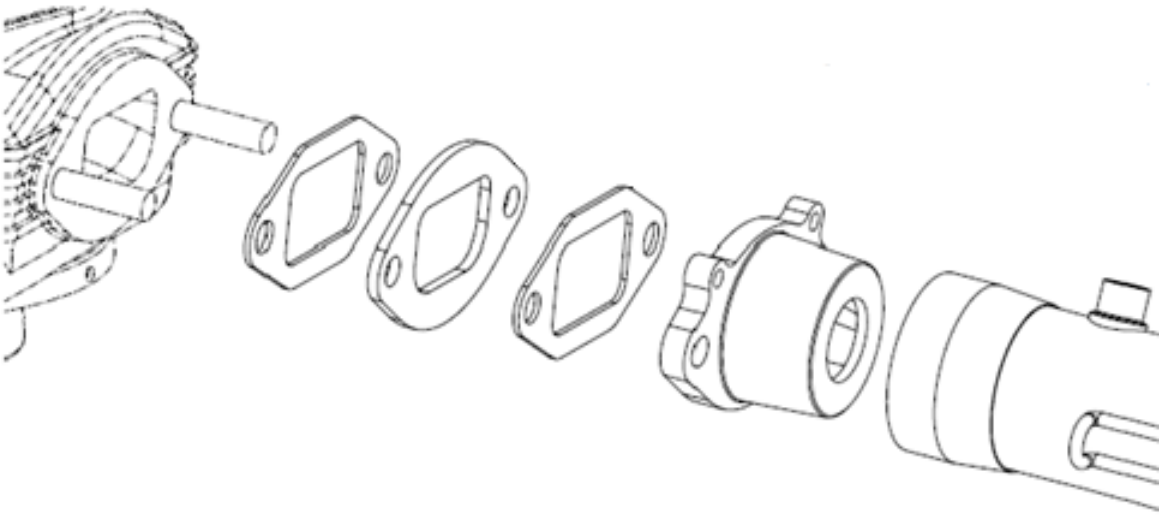

Figure 13. Details of the exhaust system taken into consideration in the present simulations [38].

The result (Figure 14) expected is that there would be a shift in the power curve in terms of the function of the length. For a longer header, peak power is located at lower rpm and vice versa; this is the result which was obtained by the simulations.

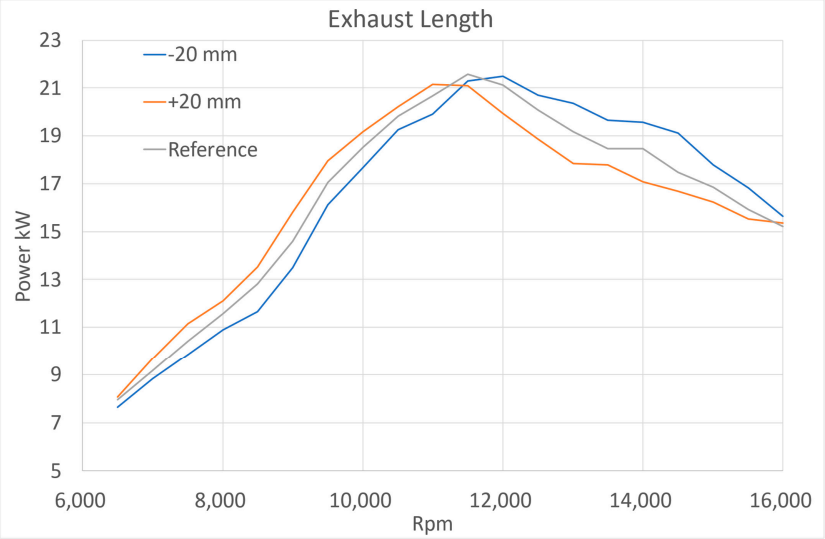

Figure 14. Comparison of the power curve for three different lengths of the exhaust header length.

3.2. Engine 2: IAME KZ Engine

The IAME Screamer III is a racing engine used for the national and world championship of the 125cc KZ class; it has a gearbox with six speeds, 54 mm bore, 54.4 mm stroke, and an intake reed valve. It is different from the X30 engine which has five transfer ports, port timing, and a combustion chamber, which are all quite different. The homologation form is in demonstrated in [39]. All the data not reported in the homologation form together with the power curve are confidential and are reported as normalized values. An image of the engine and its specifications is shown in Figure 15.

TECHNICAL DATA	
MODEL	Screamer III - KZ/KZ2
DESCRIPTION	Single cylinder – 2 stroke
CLASS	CIK/FIA - KZ/KZ2
BORE	Ø 54.00mm
MAX. BORE	Ø 54.08mm
STROKE	54.40mm
DISPLACEMENT	124.59cc
PORTS	5
INLET SYSTEM	Reed Valve
LUBRICATION	Oil mixture
IGNITION SYSTEM	Analogic
TRANSMISSION	6 Speed Gearbox
COOLING SYSTEM	Water
BALANCER SHAFT	-
STARTER	Push Start
CARB. MODEL	Dell'Orto VHSH 30
MAX. POWER	-
MAX. TORQUE	-
MAX. RPM LIMIT	-

Figure 15. The IAME Screamer III engine and its specifications [39].

Figure 16 reports a comparison between the measured power curve and the model results. Also, in this case, this is in good accordance with all the curves, and the root mean square error is about 0.5 kW.

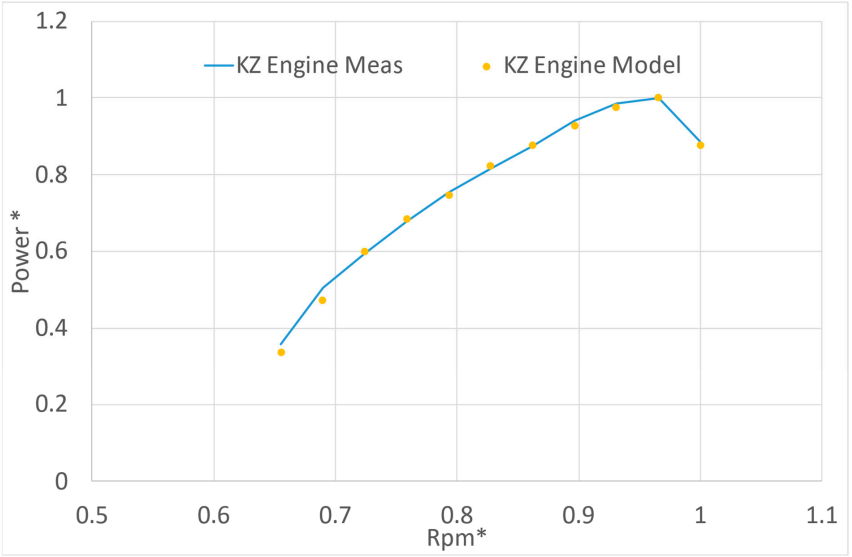

Figure 16. Comparison of measured results of IAME Screamer III with the model results in normalized form.

4. Conclusions

In this work, an engine simulation code was developed and applied to two-stroke engines. The focus was set on the turbulent combustion process, the *K-k-ϵ* turbulence model, and on the one-dimensional model which is able to take into account the area variation to minimize the mass conservation error and to reduce the role of the experimental data needed to calibrate the models; these data are not always available, especially in motorsport applications, as there are many small companies without big budgets.

The combustion process was modeled in three parts: the first, the early part, is governed by the laminar combustion speed and growth to be turbulent, the second, the fully turbulent speed, and the last, the end combustion where the interaction to the head piston and cylinder walls reduces the combustion speed to be laminar.

The turbulence model [14] was applied to two-stroke engines:

- It was refined using the momentum equation to calculate the intake energy with the advantage of reducing the influence of calibration constants, as applied in [14].
- The added term $+\frac{2}{3}\cdot K\cdot\frac{\dot{\rho}}{\rho}$ in the mean flow model, as reported in [30], increases the kinetic energy during compression and provides more accuracy when modeling high-speed engines.
- A Tumble coefficient was calculated to be used for two-stroke loop-scavenged engines. Such calculation a reduces, though it does not nullify, the need for experimental data and allows the modeling of such engines with a good accuracy.
- The calculation of the geometric length scale was refined and directly correlated with the reduction in the transfer port height; experimental data were also important in this case.

The Riemann solver of ROE, applied to one-dimensional Euler equations, was refined by modifying the source terms treatment and, in particular, the area variation, which is quite common in racing engines, especially in two-stroke ones. With the developed improvements, such a model is also able to treat abrupt area variations. The pipe end boundaries, calculated using the method of characteristics, are a source of inaccuracies, especially in mass conservation during backflow. Such a model was refined by modifying the hypothesis of linear interpolation between the last (or the first) two nodes, reducing the mass conservation error always below 0.5%.

This code was assessed by comparing its result with the experimental data of two racing two-stroke engines with different characteristics: one direct drive mono-brand engine, the IAME X30, both for senior and junior class, and a gearbox 125 cc engine, the IAME Screamer III. There is good accordance between the model and measurement, and the root mean square error for both engines is about 0.5 kW.

However, the need of calibration data, without which the results cannot be accurate, is still the main limitation of this study. By using quasi-dimensional codes for in-cylinder processes and one-dimensional codes for manifolds, the discharge coefficients and the scavenging process contain coefficients that need to be determine experimentally. In the present work, such data were found in [7,8,19], where a large number of data are reported. Also, the turbulence and the combustion models contain some coefficients and, even if first approximation values were provided, a calibration with the experimental data of a 3D model would improve their accuracies.

Author Contributions: Conceptualization, F.O. and A.B.; methodology, F.O.; software, F.O.; validation, A.B.; resources, F.O.; data curation, F.O.; writing—original draft preparation, F.O.; writing—review and editing, A.B. All authors have read and agreed to the published version of the manuscript.

Funding: This research received no external funding.

Data Availability Statement: Data are unavailable due to restrictions.

Conflicts of Interest: The authors declare no conflict of interest.

Nomenclature

A^b_{lat}	Cylinder wall area wetted by the burned zone; m^2.
A_f	Flame front surface area m^2.
A^{tot}_{lat}	Total cylinder walls area m^2.
A_{Piston}	Piston area m^2.
C_{L_g}	Calibration coefficient for geometric length scale m.
C_S	Calibration coefficient for turbulent combustion speed.
C_{T0}	Calibration coefficient for Tumble ratio.
C_{Tumble}	Tumble ratio.
c_v	Specific heat at constant volume J/Kg × K.
C_{wall}	Calibration coefficient.
E_{in}	Incoming kinetic energy rate J/s.
E	Internal Energy J/kg.
FDF	Flame development factor.
G	Friction term.
h	Enthalpy J/kg.
H	Instantaneous height of the cylinder m.
$H_{maxLift}$	Maximum intake port lift m.
$K = \frac{1}{2} \cdot m \cdot vel^2_{mean}$	Mean flow kinetic energy J.
k	Turbulent kinetic energy J.
L	Momentum kgm/s.
L_g	Geometric length scale m.
l_T	Integral scale of the turbulence m.
m	Mass kg.
m_b	Burned mass kg.
m_{mcr}	Crevices mass.
m_{ex}	Exhaust mass flowrate kg/s.
$\dot{m}_{sq}$	Squish mass flow kg.
m_{tot}	Total mass in the cylinder kg.
P_{in}	Pressure at the intake port Pa.
P_{cyl}	Cylinder Pressure Pa.
P_{Shear}	Turbulent energy production by the mean flow J/s.
P_{sq}	Turbulent energy production by the squish flow J/s.
P_{Tumble}	Turbulent kinetic energy due to the tumble; J/s.
P_ϵ	Production term of rate of dissipation of turbulent kinetic energy J/s^2.
Q	Heat Transfer term.
R	Gas constant.
Re	Reynolds number.
Re_T	Turbulent Reynolds number.

Rpm	Revolutions per minute.
r_{Tumble}	Tumble radius m.
S_T	Turbulent combustion speed m/s.
T	Temperature K.
u	Internal energy j/kg.
u'	Turbulent intensity m/s.
u_T	Combustion speed m/s.
V	Volume m^3.
v_{lam}	Laminar speed m/s.
vel_{mean}	Mean flow speed m/s.
vel_{sq}	Squish speed.
vel_{Tumble}	Tumble Speed m/s.
w_{wall}	Wall effect during the end of the combustion.
X_{air}	Air Mass fraction.
X_{fuel}	Fuel Mass fraction.
ϵ	Rate of dissipation of turbulent kinetic energy J/s.
$\tau = \frac{l_T}{u'}$	Characteristic time s.
τ_f	Tumble friction rate Nm/s^2.
ω_{Tumble}	Tumble angular speed rad/s.
ρ	Gas density kg/m^3.
ρ_{in}	Density at the intake port kg/m^3.
ν_t	Turbulent viscosity.
λ_k	Eigenvalues, characteristic speeds m/s.
ν_k	Local Courant number.

References

1. Krishna, A.S.; Mallikarjuna, J.M.; Kumar, D. Effect of engine parameters on in-cylinder flows in a two-stroke gasoline direct injection engine. *Appl. Energy* **2016**, *176*, 282–294. [CrossRef]
2. Torelli, R.; Som, S.; Pei, Y.; Zhang, Y.; Traver, M. Influence of fuel properties on internal nozzle flow development in a multi-hole diesel injector. *Fuel* **2017**, *204*, 171–184. [CrossRef]
3. Mondal, S.; Torelli, R.; Lusch, B.; Milan, P.J.; Magnotti, G.M. Accelerating the Generation of Static Coupling Injection Maps Using a Data-Driven Emulator. *SAE Int. J. Adv. Curr. Prac. Mobil.* **2021**, *3*, 1408–1424. [CrossRef]
4. Ramos, J.J. *Internal Combustion Engine Modeling*; Hemisphere Publishing Corporation: London, UK, 1989; ISBN 0-89116-157.
5. Winterbone, D.E.; Pearson, R.J. *Theory of Engine Manifold Design: Wave Action Methods for Ic Engines*; Professional Engineering Publication: Pittsburg, KS, USA, 2000.
6. van Leersum, J. A numerical model of a high performance two-stroke engine. *Appl. Numer. Math.* **1998**, *27*, 83–108. [CrossRef]
7. Blair, G.P. *Design and Simulation of Two Stroke Engines, R161, 1996-02-01*; Product Code of R-161; SAE International: Pittsburgh, PA, USA, 1996; 656p, ISBN 978-1-56091-685-7. [CrossRef]
8. Blair, G.P. *Design and Simulation of Four Stroke Engines, R-186, 1999-08-15*; Product Code of R-186; SAE International: Pittsburgh, PA, USA, 1999; ISBN 978-0-7680-0440-3. [CrossRef]
9. Available online: https://www.fiakarting.com/page/fia-karting-categories (accessed on 27 May 2023).
10. Ortenzi, F.; Vesco, E. *An Improved Multi-Pipe Junction Model for Engine Thermodynamic and Gas Dynamic Simulations*; SAE Technical Paper 2013-24-0069; SAE International: Pittsburgh, PA, USA, 2013. [CrossRef]
11. Ortenzi, F. *Modello del Sistema di Ricarica Elettrica e Termica al Capolinea e Progettazione e Sperimentazione al Banco del Sistema di Accumulo Inerziale e di Bordo*; Report RdS/PTR2020/LA2.30; SAE International: Pittsburgh, PA, USA, 2020.
12. Verhelst, S.; Sheppard, C. Multi-zone thermodynamic modelling of spark-ignition engine combustion—An overview. *Energy Convers. Manag.* **2009**, *50*, 1326–1335. [CrossRef]
13. De Bellis, V.; Bozza, F.; Tufano, D. *A Comparison between Two Phenomenological Combustion Models Applied to Different SI Engines*; SAE Technical Paper 2017-01-2184; SAE International: Pittsburgh, PA, USA, 2017. [CrossRef]
14. Fogla, N.; Bybee, M.; Mirzaeian, M.; Millo, F.; Wahiduzzaman, S. Development of a K-k-∈ Phenomenological Model to Predict In-Cylinder Turbulence. *SAE Int. J. Engines* **2017**, *10*, 562–575. [CrossRef]
15. Mohanraj, R.; Neumeier, Y.; Zinn, B.T. Characteristic-Based Treatment of Source Terms in Euler Equations for Roe Scheme. *AIAA J.* **1999**, *37*, 417–424. [CrossRef]
16. Mohanraj, R.; Neumeier, Y.; Zinn, B. Modification of Roe's Riemann Solver for the Euler Equations with Source Terms. In Proceedings of the 34th Aerospace Sciences Meeting and Exhibit, Reno, NV, USA, 15–18 January 1996. [CrossRef]
17. Roe, P.L. Characteristic-Based Schemes for the Euler Equations. *Annu. Rev. Fluid Mech.* **1986**, *18*, 337–365. [CrossRef]

18. Fleck, R.; Cartwright, A.; Thornhill, D. *Mathematical Modelling of Reed Valve Behaviour in High Speed Two-Stroke Engines*; SAE Technical Paper 972738; SAE International: Pittsburgh, PA, USA, 1997. [CrossRef]
19. Fleck, B.J.; Fleck, R.; Kee, R.J.; Chatfield, G.F.; O Mackey, D. *Validation of a Computer Simulation of a High Performance Two-Stroke Motorcycle Racing Engine*; SAE Technical Paper 2004-01-3561; SAE International: Pittsburgh, PA, USA, 2004. [CrossRef]
20. Dave, A.; Siddiqui, A.; Probst, D.; Hampson, G.J. *Development of a Reed Valve Model for Engine Simulations for Two-Stroke Engines*; SAE Technical Paper 2004-01-1455; SAE International: Pittsburgh, PA, USA, 2004. [CrossRef]
21. Caton, J. *An Introduction to Thermodynamic Cycle Simulations for Internal Combustion Engines*; John Wiley & Sons: Chichester, UK, 2015; ISBN 9781119037569.
22. Poulos, S.G.; Heywood, J.B. *The Effect of Chamber Geometry on Spark-Ignition Engine Combustion*; SAE Technical Paper 830334; SAE Transactions: New York, NY, USA, 1983. [CrossRef]
23. Vancoillie, J.; Sileghem, L.; Verhelst, S. Development and validation of a quasi-dimensional model for methanol and ethanol fueled SI engines. *Appl. Energy* **2014**, *132*, 412–425. [CrossRef]
24. Liu, K.; Burluka, A.; Sheppard, C. Turbulent flame and mass burning rate in a spark ignition engine. *Fuel* **2013**, *107*, 202–208. [CrossRef]
25. Abdel-Gayed, R.G.; Bradley, D.; Lawes, M. Turbulent burning velocities: A general correlation in terms of straining rates. *Proc. R. Soc. Lond. A Math. Phys. Sci.* **1987**, *414*, 389–413. [CrossRef]
26. Burke, E.M.; Güthe, F.; Monaghan, R.F.D. A Comparison of Turbulent Flame Speed Correlations for Hydrocarbon Fuels at Elevated Pressures. In Proceedings of the ASME Turbo Expo 2016: Turbomachinery Technical Conference and Exposition, Volume 4B: Combustion, Fuels and Emissions, Seoul, Republic of Korea, 13–17 June 2016; ASME: Reston, VA, USA, 2016. [CrossRef]
27. Bozza, F.; Teodosio, L.; De Bellis, V.; Fontanesi, S.; Iorio, A. A Refined 0D Turbulence Model to Predict Tumble and Turbulence in SI Engines. *SAE Int. J. Engines* **2019**, *12*, 15–30. [CrossRef] [PubMed]
28. Kim, M.; Kim, Y.; Kim, J.; Song, H.H. Development of quasi-dimensional turbulence model for spark-ignition engine with physical analysis of tumble: Energy-based tumble model focusing on energy intake and turbulence production. *Appl. Energy* **2019**, *252*, 113455. [CrossRef]
29. Dai, W.; Newman, C.E.; Davis, G.C. *Predictions of In-Cylinder Tumble Flow and Combustion in SI Engines with a Quasi-Dimensional Model*; SAE Technical Paper 961962; SAE International: Pittsburgh, PA, USA, 1996. [CrossRef]
30. Dulbecco, A.; Richard, S.; Laget, O.; Aubret, P. *Development of a Quasi-Dimensional K-k Turbulence Model for Direct Injection Spark Ignition (DISI) Engines Based on the Formal Reduction of a 3D CFD Approach*; SAE Technical Paper 2016-01-2229; SAE International: Pittsburgh, PA, USA, 2016. [CrossRef]
31. Glaister, P. An approximate linearised riemann solver for the three-dimensional euler equations for real gases using operator splitting. *J. Comput. Phys.* **1988**, *77*, 361–383. [CrossRef]
32. Toro, E.F. *Riemann Solvers and Numerical Methods for Fluid Dynamics—A Practical Introduction*; Springer: Berlin/Heidelberg, Germany, 2009; ISBN 978-3-540-25202-3. [CrossRef]
33. Benson, R.S. *The Thermodynamics and Gas Dynamics of Internal-Combustion Engines*; Clarendon Press: Oxford, UK, 1982; Volume 1–2.
34. Serrano, J.R.; Arnau, F.; Piqueras, P.; Belmonte, M.A.R. Assessment of a methodology to mesh the spatial domain in the proximity of the boundary conditions for one-dimensional gas dynamic calculation. *Math. Comput. Model.* **2010**, *54*, 1747–1752. [CrossRef]
35. Mackey, D.O.; Crandall, J.G.; Chatfield, G.F.; Ashe, M.C. *Optimization of Exhaust-Pipe Tuning on a 4-Stroke Engine Using Simulation*; SAE Technical Paper 2002-01-0002; SAE Transactions: New York, NY, USA, 2002. [CrossRef]
36. Sun, X.; Liu, H.; Duan, X.; Guo, H.; Li, Y.; Qiao, J.; Liu, Q.; Liu, J. Effect of hydrogen enrichment on the flame propagation, emissions formation and energy balance of the natural gas spark ignition engine. *Fuel* **2022**, *307*, 121843. [CrossRef]
37. Duan, X.; Liu, Y.; Liu, J.; Lai, M.-C.; Jansons, M.; Guo, G.; Zhang, S.; Tang, Q. Experimental and numerical investigation of the effects of low-pressure, high-pressure and internal EGR configurations on the performance, combustion and emission characteristics in a hydrogen-enriched heavy-duty lean-burn natural gas SI engine. *Energy Convers. Manag.* **2019**, *195*, 1319–1333. [CrossRef]
38. IAME X30 Homologation Form. Available online: https://x30promotion.com/regolamento/ (accessed on 27 May 2023).
39. Iame Screamer III KZ Homologation Form. Available online: https://www.iamekarting.com/homologations/ (accessed on 27 May 2023).